

TSE-Net: Semi-supervised Monocular Height Estimation from Single Remote Sensing Images

Sining Chen^{a,b}, Xiao Xiang Zhu^{a,b}

^a*Chair of Data Science in Earth Observation, Technical University of Munich (TUM), Munich, 80333, Germany*

^b*Munich Center for Machine Learning (MCML), Munich, 80538, Germany*

Abstract

Monocular height estimation plays a critical role in 3D perception for remote sensing, offering a cost-effective alternative to multi-view or LiDAR-based methods. While deep learning has significantly advanced the capabilities of monocular height estimation, these methods remain fundamentally limited by the availability of labeled data, which are expensive and labor-intensive to obtain at scale. The scarcity of high-quality annotations hinders the generalization and performance of existing models. To overcome this limitation, we propose leveraging large volumes of unlabeled data through a semi-supervised learning framework, enabling the model to extract informative cues from unlabeled samples and improve its predictive performance. In this work, we introduce TSE-Net, a self-training pipeline for semi-supervised monocular height estimation. The pipeline integrates teacher, student, and exam networks. The student network is trained on unlabeled data using pseudo-labels generated by the teacher network, while the exam network functions as a temporal ensemble of the student network to stabilize performance. The teacher network is formulated as a joint regression and classification model: the regression branch predicts height values that serve as pseudo-labels, and the classification branch predicts height value classes along with class probabilities, which are used to filter pseudo-labels. Height value classes are defined using a hierarchical bi-cut strategy to address the inherent long-tailed distribution of heights, and the predicted class probabilities are calibrated with a Plackett-Luce model to reflect the expected accuracy of pseudo-labels. We evaluate the proposed pipeline on three datasets spanning different resolutions and imaging modalities: the ISPRS Vaihingen dataset (IR-R-G aerial images, 0.09 m resolution), the SynRS3D

dataset (synthetic images, 0.6–1 m resolution), and the GBH dataset (satellite RGB images, 3 m resolution). Experimental results demonstrate that our approach consistently outperforms baseline methods, and ablation studies confirm the contribution of each design component. Codes are available at <https://github.com/zhu-xlab/tse-net>.

Keywords: monocular height estimation, semi-supervised learning, long-tailed distribution, teacher-student network

1. Introduction

Monocular height estimation from single remote sensing images produces height maps delivered as normalized digital surface models (nDSMs). These maps are crucial for a wide range of downstream applications, including 3D building modeling in urban areas [1, 2] and canopy height models in forests [3, 4]. As buildings are among the most prominent man-made structures, their 3D representations enhance our understanding of anthropogenic processes such as urbanization [5], population dynamics [6], and energy exchange [7]. Forests play a vital role in the global carbon cycle, and therefore, accurate canopy height models are indispensable for studying and mitigating climate change [8].

Height maps can also be derived from alternative techniques, such as direct 3D observations with light detection and ranging (LiDAR) [9, 10], synthetic aperture radar (SAR) [11, 12], or stereo pairs of optical images [13]. Nevertheless, single-image-based approaches offer distinct advantages, including lower costs, reduced occlusions, and improved data availability. The abundance of single-view imagery not only facilitates large-scale applications with timely updates but also enables deep learning models to leverage a vast amount of data for improved generalization.

Deep learning provides a data-driven solution to monocular height estimation, eliminating the need for handcrafted features and offering greater flexibility and representational capacity. However, the performance of such models heavily depends on the quantity and quality of labeled data. While numerous studies have explored deep-learning-based monocular height estimation [14, 15, 16, 17, 18, 19, 20, 21, 22], most rely on fully supervised learning, assuming the availability of ground-truth labels for every sample. In practice, labeled data are scarce [23, 24], as height information is typically acquired from costly 3D sensors such as LiDAR or stereo systems.

Semi-supervised learning (SSL) offers a promising solution by exploiting unlabeled data to guide network training. Among SSL techniques, consistency-based [25, 26, 27, 28, 29] and self-training-based [30, 31, 32, 33, 34] approaches have achieved state-of-the-art results and also proven effective in remote sensing applications [35, 36, 37, 38, 39, 40, 41]. However, these methods cannot be directly applied to semi-supervised monocular height estimation. First, most of them are designed for classification tasks, either image-level classification or pixel-level segmentation, where the discrete label space is inherently robust to false regularization signals from the teacher network. In contrast, for height regression, pseudo-label filtering becomes crucial to prevent error propagation. Second, height values exhibit an extremely long-tailed distribution [42], and teacher networks tend to neglect rare high-value pixels, further exacerbating underestimation in the student network.

To overcome these limitations, we propose a novel semi-supervised strategy specifically designed for monocular height estimation. Inspired by previous work that reformulates height estimation as a classification or hybrid classification-regression task [21, 22], we introduce a pseudo-label filtering mechanism based on an uncertainty proxy derived from the class probabilities of height values. To ensure that this proxy reliably reflects pseudo-label accuracy, we employ a Plackett-Luce model [43, 44] to align the ranking of class probabilities with pseudo-label errors. Furthermore, to address the long-tailed distribution of height values, we design a hierarchical bi-cut strategy that balances class samples across the entire value range and emphasizes high-value pixels during training.

In summary, this work presents the first study of semi-supervised learning for monocular height estimation. Our main contributions are as follows:

- We propose the first semi-supervised framework for monocular height estimation, introducing a self-training pipeline named TSE-Net (Teacher-Student-Exam). Unlike conventional self-training approaches, TSE-Net incorporates an additional exam sub-network that temporally aggregates the student network for improved performance stability.
- We design a joint classification-regression network as the teacher network, which generates both pseudo-labels and confidence metrics. The confidence metrics are aligned with pseudo-label errors through a Plackett-Luce model.
- We mitigate the long-tailed height distribution via a hierarchical bi-cut

strategy that balances class samples and emphasizes high-value pixels, thereby reducing systematic underestimation.

- We conduct extensive experiments and ablation studies, demonstrating the effectiveness of the proposed pipeline and validating the contribution of each design component.

The remainder of the article is organized as follows. Section 2 reviews related studies. The proposed method is described in detail in Section 3, followed by Section 4, which describes the experiments, and Section 5, which presents the experimental results. Ablation studies and discussions are presented in Section 6. Conclusions are drawn, and further research directions are described in Section 7.

2. Related Works

2.1. Monocular Height Estimation

Monocular height estimation takes a single image as input and outputs a corresponding height map. In essence, it is a dense prediction problem that can be approached through three different paradigms: regression, classification, and classification-regression.

2.1.1. Regression

Treating monocular height estimation as a regression task is the most straightforward approach, where the output space is continuous. Most methods in this category adopt encoder-decoder fully convolutional networks (FCN). As a dense regression problem, many off-the-shelf FCNs originally designed for semantic segmentation can be adapted by removing the output activation, such as FCN [45], SegNet [46], U-Net [47], and Eff-UNet [48].

Several networks have been developed specifically for monocular height estimation [14, 15, 16, 17, 18, 19, 20]. For instance, one of the earliest neural networks for this task was proposed by Mou & Zhu [15], featuring a standard encoder-decoder FCN architecture with skip connections for low-level feature fusion. Amirkolaee et al. [17] improved performance through multi-level feature fusion, and reduced computational cost with an efficient up-sampling block. Xing *et al.* [20] introduced a gated feature aggregation module (GFAM) for feature fusion and a progressive refinement module (PRM) for result refinement. Additionally, Srivastava et al. [14] explored

multi-task learning by jointly predicting height and semantic segmentation, demonstrating the benefit of incorporating semantic cues.

With the recent emergence of foundation models in computer vision, several large-scale approaches have been developed for monocular depth estimation (MDE), a closely related task. For example, DepthAnything [49, 50] introduced the first MDE foundation model, built upon DINO encoders [51] and trained on massive datasets, showing strong generalizability across diverse scenes. More recently, Marigold [52] leveraged diffusion models, enabling efficient adaptation for single-image depth inference.

2.1.2. Classification

Inspired by advances in MDE, researchers have explored reframing monocular height estimation as a classification problem. Fu et al. [53] first proposed discretizing the continuous output space into a set of ordinal classes, where each class corresponds to a height interval. The model predicts the class for each pixel, and ordinal regression is introduced to preserve the inherent ordering among classes, leading to improved performance. Li et al. [21] extended this paradigm to remote sensing, demonstrating its feasibility for monocular height estimation.

Although this classification-based formulation achieved state-of-the-art performance at that time, it introduced quantization artifacts because the final height values are typically approximated by the midpoints of the predicted class intervals.

2.1.3. Classification-Regression

To mitigate the discretization artifacts of pure classification methods, classification-regression approaches have been developed. AdaBins [54] and its successors [55, 56] combined the strengths of both paradigms by estimating height values as the expected value of class probability distributions. Moreover, they introduced adaptive bins, where class boundaries dynamically adjust to the image-specific value distribution. Inspired by these advances, Chen et al. [22] proposed HTC-DC Net, which further addressed the long-tailed distribution of height values and constrains the pixel-wise distribution, achieving state-of-the-art results in monocular height estimation.

Despite these substantial advances, existing methods generally assume the availability of sufficient labeled data for supervised training. In practice, acquiring accurate height labels is expensive and labor-intensive, underscoring the need for methods that perform well with limited annotations.

2.2. *Semi-supervised Learning*

Semi-supervised learning (SSL) addresses scenarios where labeled data samples are restrictively available but unlabeled data are abundant. State-of-the-art approaches are broadly categorized into consistency-based and self-training-based approaches.

Consistency regularization enforces that the model consistently produces predictions on the same inputs under different perturbations [25, 26, 27, 28, 29]. For example, Ouali et al. [25] proposed cross-consistency training, which regularizes intermediate representations under multiple perturbations. Wang et al. [28] conducted a feature-level consistency learning framework called Density-Descending Feature Perturbation (DDFP), which aims at effective regularization of the low-density decision boundary. Mai et al. [29] proposed RankMatch, which incorporates inter-pixel correlation under perturbations. In remote sensing, Wang et al. [35] first utilized consistency-based semi-supervised learning for semantic segmentation. Zhang et al. [36] proposed a transformation consistency regularization framework that considers various spatial transformations or perturbations. Li et al. [37] focused on feature-level perturbations for semi-supervised building footprint generation.

On the other hand, self-training expands the effective training set by including pseudo-labels for the unlabeled data samples [30, 31, 32, 33, 34]. FixMatch [30] is one of the most influential self-training semi-supervised learning frameworks, where weak and strong augmentations are applied to create two distinct views of the same image, and pseudo-labels from the weak view supervise the strong one. In this context, pseudo-label filtering is crucial. FixMatch conducts filtering via a fixed threshold, whereas later works, such as FlexMatch [31] and SoftMatch [32], introduced adaptive or dynamic thresholds for different classes. In remote sensing, Zhang et al. [38] employed a joint self-training pipeline for semi-supervised change detection. Huang et al. extended self-training for semantic segmentation with adaptive matching [39], decoupling and weighting strategies [40], and debiasing mechanisms [41].

Despite these advantages, the SSL approaches are developed for classification or segmentation tasks with discrete outputs. In contrast, regression problems such as monocular height estimation remain underexplored. This gap motivates the development of dedicated SSL frameworks tailored for continuous-value prediction tasks.

3. Methodology

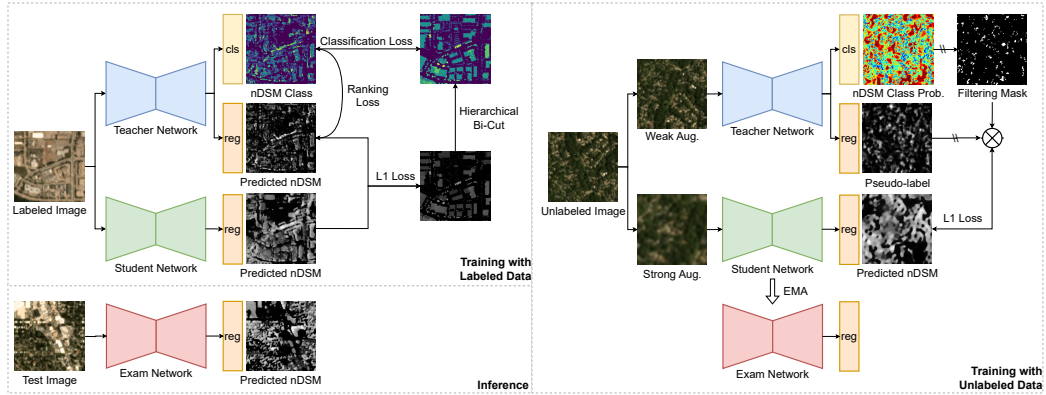


Figure 1: TSE-Net Pipeline. The framework consists of three networks: the teacher (T), student (S), and exam (E) networks. The teacher network is a classification-regression multi-task network, where the class probabilities are calibrated to align with the regression errors via a Plackett-Luce model. The student and exam networks share the same regression architecture. On the labeled dataset, the teacher and student networks are jointly trained using the ground truth labels. On the unlabeled dataset, two views—a weak and a strong augmentation—are fed into the teacher and student networks, respectively. The teacher produces pseudo-labels that are filtered by class probabilities to supervise the student network. The exam network is updated as the exponential moving average (EMA) of the student network. During inference, only the exam network is used.

As illustrated in Fig. 1, the design of TSE-Net follows the self-training pipeline, with two innovations specific to the monocular height estimation task. First, an additional network, termed the exam network, accumulates the weights of the student network via exponential moving average (EMA) updates to maintain temporally stabilized performance. Second, the teacher network is designed as a multi-task architecture with an additional classification branch, which mitigates the long-tailed distribution problem and provides probabilities that serve as proxies for pseudo-label filtering.

3.1. Teacher-Student-Exam Self-training

Following the self-training paradigm, the pipeline includes two primary networks: the teacher and student. Both networks are trained simultaneously on the labeled dataset, while during training they are also exposed

to unlabeled data in two different views, strong augmentations for the student network, and weak ones for the teacher. The teacher network predicts pseudo-labels for the unlabeled samples to supervise the student network, thus allowing the student to learn from data with greater diversity.

Conventionally, the teacher network maintains a temporal ensemble of the student network via EMA updates. However, our experiments indicate that when the teacher network differs slightly in architecture and objectives from the student, it may not represent the optimal state of the student. Therefore, we introduce an exam network that maintains a temporal ensemble of the student while sharing the same architecture and objective. The exam network is updated only as the EMA of the student’s weights and is not updated through gradient backpropagation.

To generate two different data views for training, weak and strong augmentations are applied to unlabeled data samples. The weak augmentations involve subtle geometric transformations that do not alter scale or spectral patterns, including random flipping and 90-degree rotations. The strong augmentations include geometric and spectral transformations, such as random rotations with arbitrary angles, random cropping to half size, random gamma, brightness, and contrast adjustments, and random Gaussian blurring.

3.2. Multi-task Network as Teacher

The teacher network is designed as a multi-task model comprising a classification and a regression branch. The regression branch predicts pixel-wise height values, while the classification branch predicts pixel-wise height classes defined by the hierarchical bi-cut. This multi-task design serves two purposes: first, the classification branch provides per-pixel class probabilities that are used for pseudo-label filtering. Second, discretizing the continuous output space in a balanced way mitigates biases caused by the long-tailed data distribution.

3.2.1. Architecture

The multi-task network adopts an encoder-decoder structure. The encoder processes the input image to extract condensed feature representations, which are then upsampled by the decoder to match the input image. The resulting feature tensor is fed into a regression output layer to predict height values and transformed by a linear layer into classification features, which

are used by the classification output layer to predict height classes for each pixel.

3.2.2. Hierarchical Bi-Cut for Classification Branch

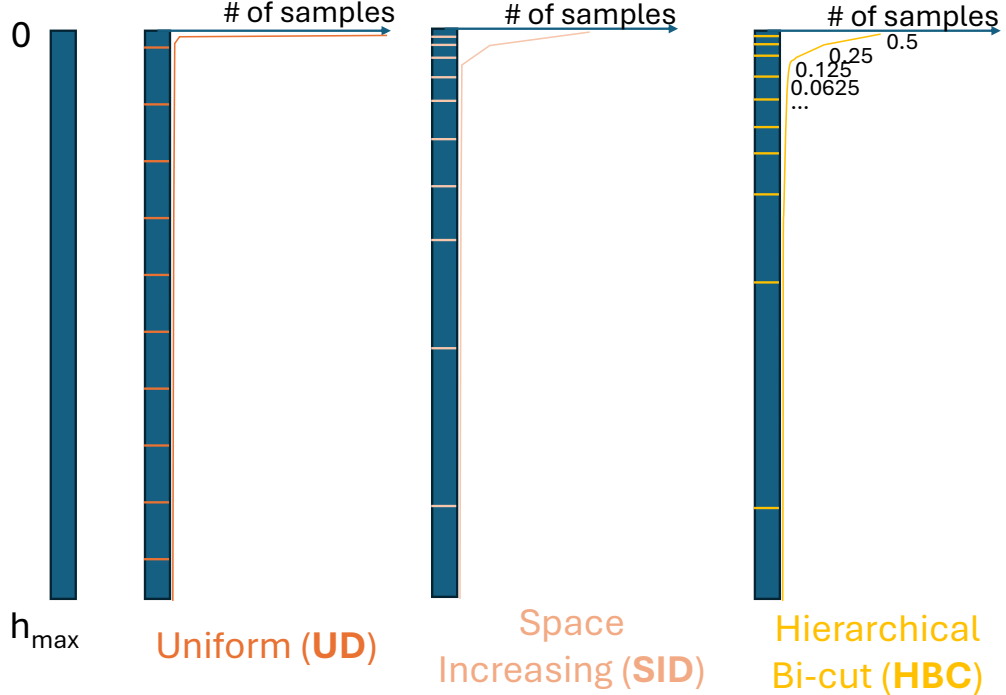


Figure 2: Different discretization strategies for converting regression to classification. h_{\max} : maximal height value in the dataset. Uniform discretization (UD): divides the height range uniformly. Space-increasing discretization (SID): divides the height range logarithmically. Hierarchical Bi-cut (HBC): divides the height range hierarchically so that each cut splits the samples in half.

To transform the regression problem into a classification one, the continuous output space $H = (h_{\min}, h_{\max})$ is discretized into N bins. Previous works on monocular depth and height estimation employed three main strategies (see Fig. 2):

- **Uniform Discretization (UD):** Divides the height range evenly: The lower bin edge for class i is

$$e_i = h_{\min} + \frac{h_{\max} - h_{\min}}{N}i. \quad (1)$$

- **Space-Increasing Discretization (SID)** [53], also referred to as **Log-Uniform Discretization** in [55]: Applies uniform division in logarithm space to have increased intervals of large height/depth values: The lower bin edge for class i is written as

$$e_i = \exp(\log h_{\min} + \frac{\log h_{\max} - \log h_{\min}}{N} i). \quad (2)$$

- **Adaptive Bins (AdaBins)** [55]: Learns bin edges adaptively for each image according to its height value distribution.

Unlike depth values in monocular depth estimation, height values in monocular height estimation are extremely long-tailed [42] (see Fig. 3). For example, in the GBH dataset, pixels lower than 1 m account for over half of all pixels, whereas high-value pixels are sparse. Improper class definitions can thus lead to strong model bias and degrade classification accuracy. From this perspective, UD fails to consider the data distribution. More specifically, when the number of classes is relatively small, the first class will encompass almost all the pixels, which makes the classification meaningless. SID partly addresses the issue, but lacks adaptability to the dataset. AdaBins adapts to each image, but is computationally more complex, and the classes across images are not consistent, which poses challenges when filtering the pseudo-labels based on the class probabilities. Furthermore, under semi-supervised learning settings where labeled samples are limited, some classes defined by UD or SID may never appear during training.

To overcome these limitations, we proposed Hierarchical Bi-Cut (HBC), which recursively divides the height range into halves. The class edges, termed HBC-points, are defined iteratively. The first HBC-point divides the full range at the median height value, separating height values for class 0 and the remaining classes. Subsequent cuts divide the remaining upper ranges by their medians until all classes from 1 to $N - 1$ are defined. Formally, the i -th HBC-point Q_i , separating class i from higher classes, is defined as

$$Q_i : P(h < Q_i) = 1 - (\frac{1}{2})^{i+1}, \quad (3)$$

where h is the pixel height value. In practice, the HBC-points are defined for a dataset once by a binary search. This hierarchical approach balances each binary split between the lower class and the remaining higher classes, addressing the imbalance problem without adding computational overhead.

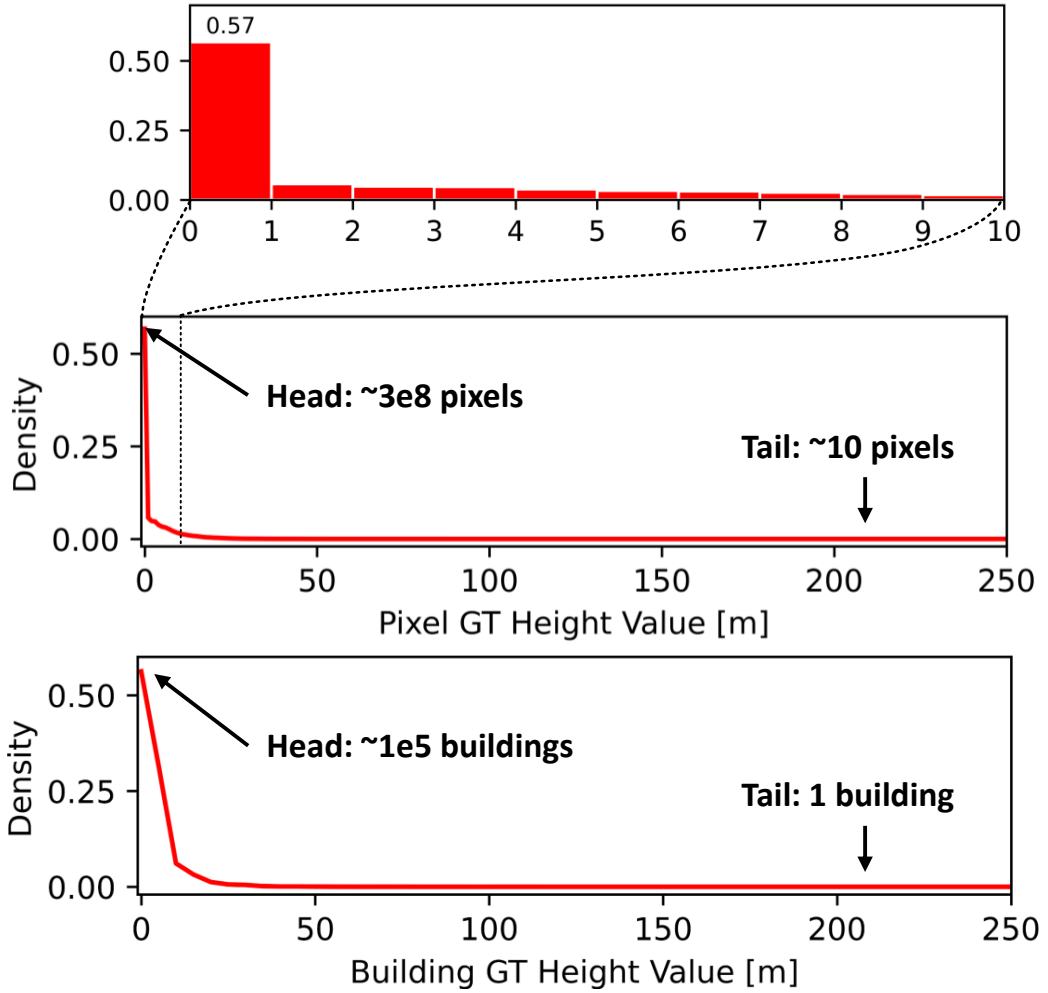


Figure 3: Height value Distribution of the GBH training and validation Sets. The distribution exhibits a pronounced long-tailed pattern: approximately $3e8$ pixels (57 % of the total) fall within background regions below 1 m, while the frequency of pixels at larger heights decreases sharply to about 10 pixels per 1 m bin. A similar long-tailed distribution is observed for the building ground-truth height values.

Following HBC, the imbalanced classification problem is decomposed into $N - 1$ binary classification tasks, naturally aligning with ordinal regression [57, 58]. For each binary classification problem, one has to decide whether a pixel belongs to this class or the following classes with higher values. Intuitively, a pixel belonging to classes with higher values than class $c + 1$ should bear a height value also higher than class c .

To implement the intuition, ordinal regression aims to learn the objective of multi-hot labels. Different from one-hot labels, where only the ground truth class itself is expected to be positive, the multi-hot labels set all the classes equal to or lower than the ground truth class as positive. That is,

$$y = [\underbrace{1, 1, \dots, 1}_c, \underbrace{0, \dots, 0}_{N-c}, 0, 0], \quad (4)$$

where y is the label for one pixel belonging to class c . The ordinal regression loss is computed as

$$L_{cls} = \frac{1}{N-1} \sum_{i=0}^{N-1} (-y_i \log p_i - (1 - y_i) \log(1 - p_i)), \quad (5)$$

where y_i is the i -th element of the multi-hot label y , and p_i is the i -th element of the predicted probabilities p .

For pseudo-label filtering, the class probability of class i is computed as

$$q_i = \begin{cases} 1 - p_0, & i = 0, \\ (1 - p_i) \prod_{c=0}^{i-1} p_c, & 1 \leq i \leq N - 2, \\ \prod_{c=0}^{N-1} p_c, & i = N - 1. \end{cases} \quad (6)$$

3.2.3. Regression Branch

The regression branch is supervised using the L1 loss. For one pixel, that is

$$\mathcal{L}_{reg} = |\hat{h} - h|. \quad (7)$$

where \hat{h} is the predicted height value, and h is the ground truth height value.

3.2.4. Alignment of Classification Probabilities via Plackett-Luce Model

Since class probabilities are used for pseudo-label filtering, they should ideally correlate with pseudo-label accuracy: larger regression errors should correspond to lower class probabilities. To this end, we employ a Plackett-Luce (PL) model [43, 44] to enforce ranking consistency between classification probabilities and pseudo-label errors.

The PL model is a model for ranking data working with listwise preferences. Given a list of M pixels from the pseudo-labels predicted by the teacher network, their class probabilities are denoted as

$$\mathbf{q} = \{q_0, q_1, \dots, q_{M-1}\}, \quad (8)$$

and their pseudo-label absolute errors are denoted as

$$\epsilon = \{\epsilon_0, \epsilon_1, \dots, \epsilon_{M-1}\}, \quad (9)$$

where

$$\epsilon_j = |h_j - \hat{h}_j| \quad (10)$$

is the absolute error of pixel j , that is, the absolute difference between the ground truth and predicted height values of pixel j , h_j and \hat{h}_j , respectively. The PL model is designed to align the ranking of \mathbf{q} with that of ϵ .

The process is achieved by a loss function representing the negative log-likelihood of a random permutation of \mathbf{q} . The probability of a permutation π of $\arg \mathbf{q}$ is given by

$$P(\pi \mid \mathbf{q}) = \prod_{j=0}^{M-2} \frac{q_{\pi_j}}{\sum_{k=j}^{M-1} q_{\pi_k}}. \quad (11)$$

Given the ground truth permutation Π which reflects the ranking of ϵ , the probability is written as

$$P(\Pi \mid \mathbf{q}) = \prod_{j=0}^{M-2} \frac{q_{\Pi_j}}{\sum_{k=j}^{M-1} q_{\Pi_k}}. \quad (12)$$

The PL model is then optimized with the loss function written as the negative log-likelihood of the ground truth permutation, that is

$$\mathcal{L}_{\text{PL}} = -\log P(\Pi \mid \mathbf{q}). \quad (13)$$

3.2.5. Pseudo-Label Filtering from Ranking

Using the class probabilities, regression pseudo-labels are filtered according to their ranking. For a batch of B predicted height maps and class probability maps $\hat{\mathcal{Q}}$, the pixels are sorted by their class probabilities, yielding a normalized ranking map

$$\mathcal{R} = \frac{\text{argsort} \hat{\mathcal{Q}}}{|\hat{\mathcal{Q}}|}, \quad (14)$$

where $|\hat{\mathcal{Q}}|$ denotes the total number of pixels in $\hat{\mathcal{Q}}$. Pseudo-labels are retained for supervising the student network if their normalized ranking exceeds a ranking threshold r . The pseudo-label filtering mask \mathcal{M} is then defined as

$$\mathcal{M}_j = 1 \text{ if } \mathcal{R}_j > r \text{ else } 0, \quad (15)$$

where j is the pixel index.

The ranking threshold decays from its initial value 1 according to a factor λ during training, that is

$$r_{t+1} = \max(r_t \lambda, 0.5). \quad (16)$$

This ensures that unlabeled samples are initially excluded when the network is not well-trained and predictions are uncertain. As training progresses, the threshold decreases, gradually incorporating more unlabeled samples into the training pool. This progressive inclusion prevents network collapse caused by unreliable pseudo-labels.

3.2.6. Loss Functions

The teacher network is trained with a combined loss, consisting of the classification loss (see Eqn. 5), regression loss (see Eqn. 7), and PL model loss (see Eqn. 13), written as

$$\mathcal{L}_{\text{sup}}^T = \mathcal{L}_{\text{cls}} + \mathcal{L}_{\text{reg}}^T + \mathcal{L}_{\text{PL}} \quad (17)$$

3.3. Regression Networks as Student and Exam

The student network expands the model’s capacity to handle data with greater variability and is supervised by the filtered pseudo-labels produced by the teacher network. Given pseudo-labels \tilde{h}^T from the teacher and the filtering mask \mathcal{M} derived from ranking thresholding, the student network is trained via

$$\mathcal{L}_{\text{unlabeled}} = \mathcal{L}_{\text{reg}}^S \odot \mathcal{M} = |\hat{h}^S - \tilde{h}^T| \odot \mathcal{M}, \quad (18)$$

where \hat{h}^S represents the predictions of the student network on unlabeled data samples.

The exam network does not participate in loss computation or gradient backpropagation. Its weights are updated exclusively as the EMA of the student network. During inference and testing, the exam network is used to generate the final outputs.

In summary, the training procedure of TSE-Net is outlined in Algorithm 1.

Algorithm 1 Training Step of TSE-Net

Require: Image x , ground-truth nDSM y , unlabeled image u

- 1: $(\hat{h}^T, p^T) \leftarrow \text{Teacher}(x)$ \triangleright Teacher predictions (height and class)
- 2: $\hat{h}^S \leftarrow \text{Student}(x)$ \triangleright Student prediction (height)
- 3: $q^T \leftarrow \text{Binary2Class}(p^T)$ \triangleright Convert binary probabilities into class probabilities
- 4: $\mathcal{L}_{\text{sup}}^T \leftarrow \mathcal{L}_{\text{cls}}(p^T, \text{ndsm2cls}(h)) + \mathcal{L}_{\text{reg}}(\hat{h}^T, h) + \mathcal{L}_{\text{PL}}(q^T, \text{L1}(\hat{h}^T, h))$
- 5: $\mathcal{L}_{\text{sup}}^S \leftarrow \mathcal{L}_{\text{reg}}(\hat{h}^S, h)$
- 6: $v_1 \leftarrow \text{AugmentWeak}(u)$
- 7: $(\tilde{h}_1^T, \tilde{p}_1^T) \leftarrow \text{Teacher}(v_1)$ \triangleright Pseudo-labels
- 8: $(v_2, \tilde{h}_2^T, \tilde{p}_2^T) \leftarrow \text{AugmentStrong}(v_1, \tilde{h}_1^T, \tilde{p}_1^T)$
- 9: $\tilde{q}_2^T \leftarrow \text{Binary2Class}(\tilde{p}_2^T)$
- 10: $\mathcal{M} \leftarrow \text{rank}(\tilde{q}_2^T) > \tau_{\text{rank}}$ \triangleright Pseudo-label mask
- 11: $\hat{h}_2^S \leftarrow \text{Student}(v_2)$
- 12: $\mathcal{L}_{\text{unlabeled}} \leftarrow \mathcal{L}_{\text{reg}}^S(\hat{h}_2^S, \tilde{h}_2^T) \odot \mathcal{M}$
- 13: $\mathcal{L} \leftarrow \mathcal{L}_{\text{sup}}^T + \mathcal{L}_{\text{sup}}^S + \mathcal{L}_{\text{unlabeled}}$
- 14: Backpropagate \mathcal{L}
- 15: $\text{Update}(\text{Student})$ \triangleright Adam optimizer
- 16: $\text{EMA_Update}(\text{Exam, Student})$ \triangleright Exponential moving average

4. Experiments

4.1. Datasets

To validate the proposed method, three datasets are used in experiments, namely ISPRS Vaihingen, SynRS3D and GBH. These datasets cover different

Table 1: Overview of the Datasets Used for the Experiments.

Sensor	ISPRS Vaihingen [59, 60] Airborne	SynRS3D [61] Synthetic	GBH Planet
Involved Areas	Vaihingen an der Enz, Germany	n.a.	18 cities around the globe
Resolution (m/pixel)	0.09	0.6–1	5 (upsampled to 3)
Semantic Classes	Impervious, Building, Low Vegetation, Tree, Car	Bareland, Rangeland, Developed Space, Road, Tree, Water, Agriculture Land, Building	Building, Non-building
Original Image Size	$\sim 2000 \times 2000$	512×512	256×256
Cropped Image Size	256×256	512×512	256×256
Number of Cropped Images	2,838	5516	8703
Training: Validation: Test	1060:264:1514 (4:1:5)	3862:551:1103 (7:1:2)	5442:1477:1784 (6:2:2)
Labeled: Unlabeled in Training	1:1059 (0.1%) 5:1055 (0.5%) 10:1050 (1%) 53:1007 (5%) 106:954 (10%)	3:3859 (0.1%) 19:3843 (0.5%) 38:3824 (1%) 190:3672 (5%) 380:3482 (10%)	5:5437 (0.1%) 27:5415 (0.5%) 54:5388 (1%) 272:5170 (5%) 544:4898 (10%)

domains (synthetic and real), sensors (infrared and RGB), platforms (aerial and space), and spatial resolutions (from 0.09 m to 3 m). A detailed description of the datasets is provided in Table 1. Note that the ISPRS Vaihingen dataset is split so that the test set is consistent with the setting of the Data Fusion Contest. Additionally, it simulates extreme scenarios in which labeled training data are limited.

4.2. Evaluation Metrics

The methods are evaluated in terms of root mean square errors (RMSEs), computed over all pixels and across different land cover classes. To assess the models’ ability to mitigate long-tailed biases, an averaged RMSE of building heights across the full height range is also calculated. For this purpose, buildings are assumed to have Level of Detail 1 (LoD1), where a single height value is assigned to each building instance. The predicted and ground truth building heights are then defined as the median height value within each building footprint coverage. Additionally, the mean relative error is computed for each building instance to more accurately reflect the relative scale of prediction errors.

4.3. Implementation Details

U-Net [47] is set as the backbone network. The experiments are designed as follows:

- The backbone network is trained with all available data (100%), serving as an upper-bound reference for performance.
- The backbones are trained in a fully supervised manner with 0.1%, 0.5%, 1%, 5%, and 10% of the labeled data, providing baselines for varying levels of label scarcity.
- The proposed networks are trained in a semi-supervised manner using the same labeled subsets (0.1%–10%) together with the remaining unlabeled images, and the results are compared against the baselines.

All networks are trained using the Adam optimizer with a learning rate of 1e-4 for 200 epochs. The epoch yielding the best performance on the validation set is selected for testing. Each experiment is repeated three times, and the reported metrics correspond to the average across these runs.

5. Results

The quantitative results are reported in Table 2, Table 3, and Table 4, with corresponding qualitative examples shown in Fig. 4, Fig. 5, and Fig. 6.

Overall, the results confirm that performance improves as the proportion of labeled data increases. First, with more labels, the total RMSEs and relative building errors decrease across all three datasets. Second, across land cover types, those characterized by lower heights, such as impervious surfaces, low vegetation, and cars in ISPRS Vaihingen (Table 2), or bareland, rangeland, developed space, roads, water, and agricultural land in SynRS3D (Table 3), often show limited or even degraded improvement as the label proportion increases. In contrast, tall classes such as buildings and trees benefit more consistently. Third, given the long-tailed distribution of building heights, adding more labels also exposes the network to extreme values, which improves the balanced building RMSEs across all three datasets.

When unlabeled data are incorporated through the self-training pipeline, three main effects become evident, and all three suggest that unlabeled data are effectively utilized in a similar manner to labeled data. This is because the same behaviors can also be observed when the proportion of labeled data is increased, as discussed above.

First, semi-supervised learning yields substantial overall improvements, particularly at very low label proportions (0.1%–1%). For example, on

Table 2: Experiment Results on ISPRS Vaihingen. The RMSEs are reported in meters for all pixels (Total), for each land cover type, and for buildings averaged by different heights (Building Balanced). Building Relative denotes the mean relative error of building instances.

Labeled Percentage	Mode	Total	Impervious	Building	Low Vegetation	Tree	Car	Building Balanced	Building Relative
0.1	sup.	4.0747	1.4568	6.4593	1.9049	4.4689	1.5476	8.5296	0.8161
	semi	3.7562	2.2343	4.9890	2.1756	4.7172	3.6533	6.9682	0.4565
0.5	sup.	3.9268	1.5017	6.1442	1.8632	4.3729	1.8814	8.3209	0.7389
	semi	3.6847	2.0470	5.0112	3.1277	3.9757	2.4542	7.0436	0.5418
1	sup.	3.7425	1.4289	5.8168	1.8083	4.2111	1.6183	8.0985	0.6915
	semi	3.4485	1.5363	5.0094	2.8263	3.6228	1.9090	7.1249	0.5495
5	sup.	2.8503	1.3454	4.0585	2.1265	3.1928	1.3118	6.0352	0.3925
	semi	2.7620	1.3847	3.9119	2.3412	2.8683	1.4005	5.3548	0.3343
10	sup.	2.4505	1.4451	3.3051	1.8496	2.7554	1.6840	4.7989	0.3038
	semi	2.3235	1.4149	3.2383	1.5097	2.6247	1.3235	4.7284	0.2991
100	sup.	1.9210	1.0131	2.7796	1.2026	2.1381	0.9409	3.9035	0.2432

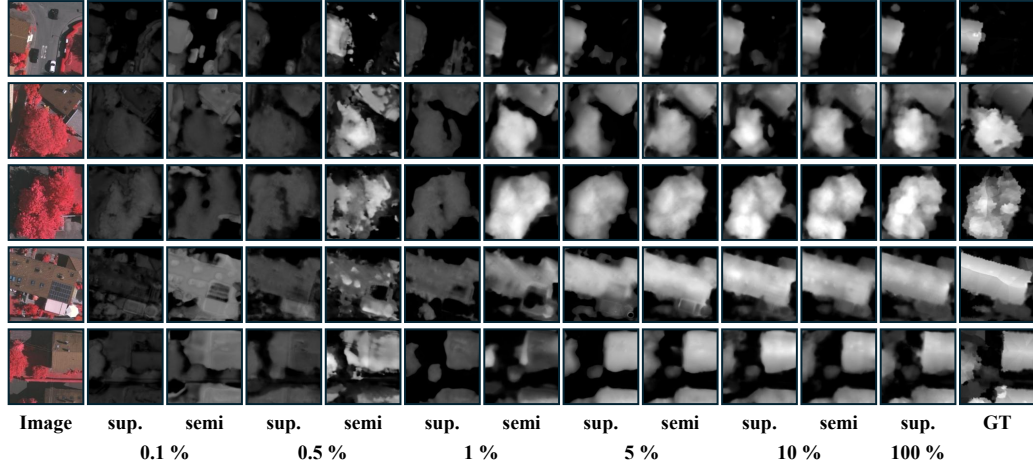


Figure 4: Qualitative results on ISPRS Vaihingen. sup.: supervised learning; semi: semi-supervised learning; GT: ground truth; percentage on the bottom denotes the labeled ratio.

Table 3: Experiment Results on SynRS3D. The RMSEs are reported in meters for all pixels (Total), for each land cover type, and for buildings averaged by different heights (Building Balanced). Building Relative denotes the mean relative error of building instances.

Labeled Percentage	Mode	Total	Bareland	Rangeland	Developed Space	Road	Tree	Water	Agriculture Land	Building	Building	
											Balanced	Relative
0.1	sup.	22.0667	0.9753	0.6789	1.8512	2.3424	8.7109	1.4581	0.8976	52.3291	49.1640	0.8973
	semi	17.8707	5.7502	3.8579	13.9634	8.7156	7.6223	5.9271	4.1192	39.8991	39.7101	0.8879
0.5	sup.	19.8165	4.1891	2.6496	6.2870	4.9685	6.4080	3.6529	2.8220	46.4933	43.7314	0.7198
	semi	15.4076	5.4603	3.1961	14.8628	7.2410	6.4711	5.3315	5.0473	33.5954	36.3823	0.8140
1	sup.	15.6627	5.9417	2.9399	11.8148	6.9981	6.3581	5.5319	3.8327	35.0818	36.2907	0.8467
	semi	14.1046	4.6899	2.9150	10.7695	4.5643	5.6551	3.7841	3.4999	31.7323	35.0314	0.7961
5	sup.	12.0842	2.9985	2.6244	8.8715	3.8812	5.0232	2.5368	2.3090	27.3505	32.5352	0.7804
	semi	10.8257	2.0875	2.0208	5.9653	2.7044	4.6858	1.5741	1.7733	24.9419	32.2449	0.6752
10	sup.	11.0390	2.5044	2.2594	6.9351	3.3501	4.5911	2.1931	2.1058	25.2400	32.0167	0.7106
	semi	9.1434	1.8249	1.9821	4.7824	2.5746	4.2950	1.4224	1.4336	20.9870	30.6148	0.6173
100	sup.	7.6350	1.6509	1.8807	4.2640	2.2845	3.7911	1.2005	1.2886	17.4010	30.1244	0.5691

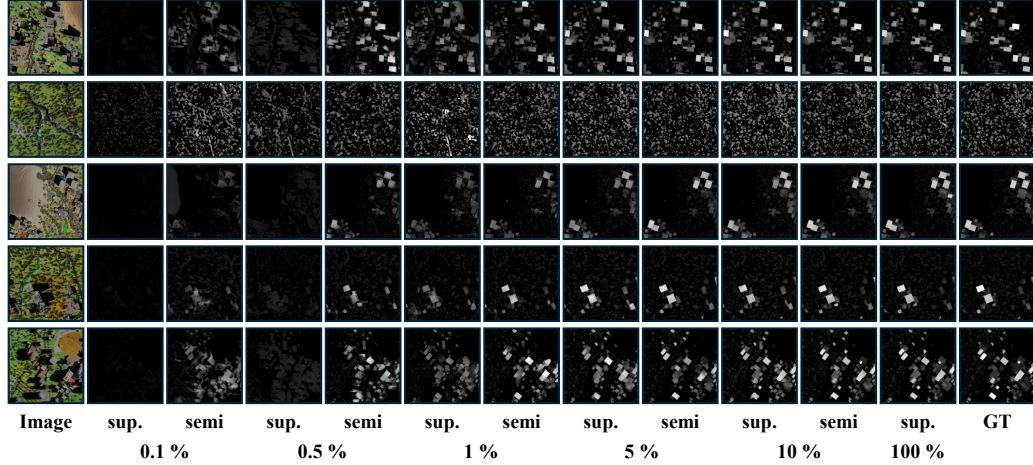


Figure 5: Qualitative results on SynRS3D. sup.: supervised learning; semi: semi-supervised learning; GT: ground truth; percentage on the bottom denotes the labeled ratio.

Table 4: Experiment Results on GBH. The RMSEs are reported in meters for all pixels (Total), for each land cover type, and for buildings averaged by different heights (Building Balanced). Building Relative denotes the mean relative error of building instances.

Labeled Percentage	Mode	Total	Non-building		Building		Building Balanced	Building Relative
			Building	Non-building	Building	Non-building		
0.1	sup.	7.2996	4.8074	13.2922	47.0171	0.7981	46.2821	0.5932
	semi	7.1086	5.0194	12.4127				
0.5	sup.	7.0267	4.6523	12.7587	47.7627	0.7350	45.6716	0.5258
	semi	6.7179	4.8258	11.5936				
1	sup.	6.5333	4.6039	11.4264	45.6464	0.5984	42.4920	0.5078
	semi	6.2725	4.8843	10.1108				
5	sup.	5.8077	4.4457	9.5237	40.2960	0.4878	40.8399	0.5022
	semi	5.7340	4.1448	9.8532				
10	sup.	5.5087	4.1569	9.1510	40.1568	0.4703	40.4248	0.4704
	semi	5.3971	4.0124	9.0781				
100	sup.	4.8920	3.8018	7.9179	37.4738	0.3845		

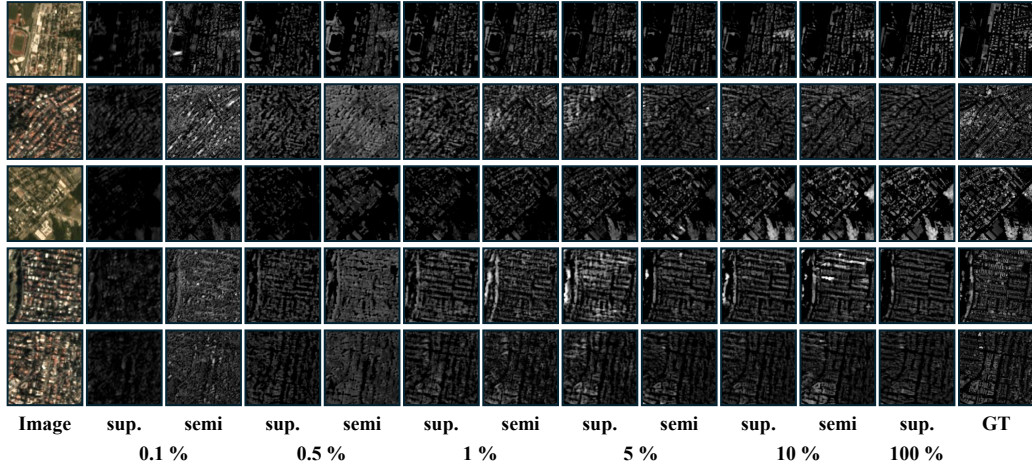


Figure 6: Qualitative results on GBH. sup.: supervised learning; semi: semi-supervised learning; GT: ground truth; percentage on the bottom denotes the labeled ratio.

the ISPRS Vaihingen dataset, the total RMSE drops from 4.0747 (supervised, 0.1%) to 3.7562 (semi-supervised, 0.1%), which corresponds to filling 14.79% of the gap towards the 100% fully supervised model. Similarly, the gaps closed on SynRS3D and GBH with only 0.1% labeled data are 29.07% and 7.93%, respectively. Furthermore, on SynRS3D (Table 3), the semi-supervised model trained with 0.1% labeled data outperforms the supervised model trained with 0.5%, and the semi-supervised model trained with 0.5% labeled data outperforms the supervised model trained with 1%. The improvements are also demonstrated by the relative building errors. In addition, these gains are reflected qualitatively: with only 0.1% labeled data, supervised predictions show no discernible structure, whereas semi-supervised predictions capture spatial context and object layout. At 0.5%–1%, supervised models start producing meaningful patterns, but semi-supervised learning further mitigates underestimation and pushes predictions closer to the ground truth.

Second, the use of unlabeled data amplifies errors for low-height classes while improving predictions for tall classes, mirroring the outcomes observed with full supervision on larger proportions of labeled data. In ISPRS Vaihingen (Table 2), RMSEs for impervious surfaces and cars increase under semi-supervised learning, while buildings and trees improve significantly. The same pattern holds in SynRS3D (Table 3), where semi-supervised models yield higher errors for rangeland and agriculture but substantially reduce errors for roads and buildings. GBH (Table 4) shows a similar contrast: non-building pixels remain stable or slightly worse, while building RMSEs improve notably, especially at 0.5 % and 1 %. The consistency of this class-dependent trade-off across all datasets underscores that unlabeled data reinforce similar learning behaviors to those driven by labeled data.

Third, unlabeled data mitigate the bias caused by the long-tailed distribution of building heights, improving balanced building RMSEs. On ISPRS Vaihingen, for instance, the balanced building RMSE decreases from 8.5296 (supervised, 0.1%) to 6.9682 (semi-supervised, 0.1%), an 18.31% improvement (Table 2). On SynRS3D, the improvement is also clear, with the balanced building RMSE dropping from 49.1640 (supervised, 0.1%) to 39.7101 (semi-supervised, 0.1%), a 19.23% improvement (Table 3). Even on GBH, where the total RMSE gain is less pronounced, the balanced building RMSE improves consistently at low label proportions (Table 4). Since similar debiasing effects are observed when more labeled data are added, these results again confirm that unlabeled data extend the training signal in a manner

consistent with labeled data.

6. Ablation Studies

Table 5: Ablation Studies on ISPRS Vaihingen (1 % labeled data). The RMSEs are reported in meters for all pixels (Total), for each land cover type, and for buildings averaged by different heights (Building Balanced). Building Relative denotes the mean relative error of building instances. The self-training pipelines are denoted in the format Teacher-Student, where the teacher and student networks are selected from: `reg`. (plain regression network), `cls`. (plain classification network), and `regcls`. (multi-task regression-classification network). For all pipelines except TSE, the teacher network is used for inference; in TSE, however, the exam network—defined as the EMA of the student—is used. Classification discretization schemes include UD (uniform discretization) and SID (space-increasing discretization).

Category	Configuration	Total	Impervious	Building	Low Vegetation	Tree	Car	Building	
								Balanced	Relative
Self-training Pipeline	reg.-reg.	3.5690	1.4624	5.4670	2.5674	3.6195	1.8846	7.7809	0.6051
	regcls.-regcls.	4.0235	1.6941	4.8137	5.2444	3.8501	1.7629	7.0092	0.4931
	regcls.-cls.	3.5718	1.9335	4.8467	3.2681	3.7583	2.8338	6.7922	0.4870
	regcls.-reg.	3.5148	2.0206	4.8726	2.9134	3.7416	2.2245	6.9466	0.5216
	regcls.-reg. (TSE)	3.4185	1.8135	4.8239	2.8901	3.5589	2.1243	6.6833	0.4737
Classification	UD	3.6065	1.6361	5.0591	3.3448	3.7305	2.1987	6.9318	0.5172
	SID	3.5476	1.6688	4.8980	3.4198	3.6494	2.0664	6.9178	0.5269
Pseudo-label Filtering	w/o PL loss	3.4655	1.4674	4.9928	2.8346	3.7535	1.6629	7.1342	0.5106
	w/o ranking	3.5520	1.7677	4.7392	3.5890	3.6755	2.1361	6.8539	0.4474
	w/o dynamic thres.	3.6958	1.8443	5.2492	3.2057	3.5340	6.2155	7.0270	0.5278
Full Configuration		3.4485	1.5363	5.0094	2.8263	3.6228	1.9090	7.1249	0.5495

In this section, ablation studies on the self-training pipeline, the classification process, and the pseudo-label filtering process are conducted, and the results are reported in Table 5, Table 6, and Table 7.

6.1. Self-training Pipeline

The self-training pipeline represents a state-of-the-art semi-supervised learning framework, typically involving a teacher and a student network. The student is updated through gradient descent, while the teacher is maintained as the EMA of the student. Labeled data directly supervise the student, whereas pseudo-labels generated by the teacher from weakly augmented views guide the student on strongly augmented views. Consequently, a pseudo-label filtering process is essential to discard unreliable pseudo-labels and stabilize the teacher’s performance during inference.

Table 6: Ablation Studies on SynRS3D (1 % labeled data). The RMSEs are reported in meters for all pixels (Total), for each land cover type, and for buildings averaged by different heights (Building Balanced). Building Relative denotes the mean relative error of building instances. The self-training pipelines are denoted in the format Teacher-Student, where the teacher and student networks are selected from: **reg.** (plain regression network), **cls.** (plain classification network), and **regcls.** (multi-task regression-classification network). For all pipelines except TSE, the teacher network is used for inference; in TSE, however, the exam network—defined as the EMA of the student—is used. Classification discretization schemes include UD (uniform discretization) and SID (space-increasing discretization).

Category	Configuration	Total	Bareland	Rangeland	Developed Space	Road	Tree	Water	Agriculture Land	Building	Building Balanced	Building Relative
Self-training Pipeline	reg.-reg.	12.1200	2.6334	2.7319	8.4961	3.5532	5.0057	1.9659	2.0365	27.5353	31.5760	0.7655
	regcls.-regcls.	15.5575	4.8723	3.2632	11.9069	6.1186	5.8625	4.1662	4.1292	35.0291	36.2192	0.8233
	regcls.-cls.	15.4924	6.2717	4.5106	12.6989	6.4734	6.2869	6.5448	5.4393	34.0093	35.4422	0.8434
	regcls.-reg.	12.9657	3.2598	3.1848	8.9516	4.3149	5.1773	2.3070	2.6106	29.4391	32.6846	0.7659
Classification	regcls.-reg. (TSE)	13.6823	3.4587	2.6387	8.4076	4.5235	5.1789	2.1375	2.4785	31.4211	34.2528	0.7618
	UD	13.4664	4.3846	2.7773	8.8040	4.1998	5.7417	3.7274	2.9660	30.5592	35.2854	0.7899
Pseudo-label Filtering	SID	13.8618	4.2508	2.6542	10.0538	4.1653	5.6254	3.4102	3.4820	31.3642	35.1998	0.7771
	w/o PL loss	14.0690	3.8011	2.8599	9.3863	4.3254	5.4906	3.2674	3.4607	32.0461	35.5205	0.7683
	w/o ranking	13.4925	2.5492	2.3617	7.0471	3.6027	5.0663	1.6986	1.9790	31.3053	34.6684	0.7469
	w/o dynamic thres.	13.1779	3.8301	2.7317	8.4527	3.8799	5.2037	2.0976	2.4370	30.1262	33.8060	0.7431
Full Configuration		14.1046	4.6899	2.9150	10.7659	4.5643	5.6551	3.7841	3.4999	31.7323	35.0314	0.7961

Table 7: Ablation Studies on GBH (1 % labeled data). The RMSEs are reported in meters for all pixels (Total), for each land cover type, and for buildings averaged by different heights (Building Balanced). Building Relative denotes the mean relative error of building instances. The self-training pipelines are denoted in the format Teacher-Student, where the teacher and student networks are selected from: **reg.** (plain regression network), **cls.** (plain classification network), and **regcls.** (multi-task regression-classification network). For all pipelines except TSE, the teacher network is used for inference; in TSE, however, the exam network—defined as the EMA of the student—is used. Classification discretization schemes include UD (uniform discretization) and SID (space-increasing discretization).

Category	Configuration	Total	Non-building	Building	Building	Building
					Balanced	Relative
Self-training Pipeline	reg.-reg.	6.4801	4.7558	11.0103	44.8061	0.5024
	regcls.-regcls.	6.7891	4.6655	12.0655	46.1828	0.5870
	regcls.-cls.	6.8870	4.7023	12.2874	46.8149	0.6321
	regcls.-reg.	6.7744	4.7510	11.8855	46.1175	0.6095
	regcls.-reg. (TSE)	6.4563	4.7717	10.9105	44.1571	0.5946
Classification	UD	6.3569	4.6251	10.8718	44.0157	0.5619
	SID	6.2037	4.6628	10.3426	42.5714	0.4922
Pseudo-label Filtering	w/o PL loss	6.3125	4.8207	10.3813	43.1037	0.4939
	w/o ranking	6.4187	4.6608	10.9934	44.5454	0.5973
	w/o dynamic thres.	6.6426	4.6827	11.6146	45.5521	0.5843
Full Configuration		6.2725	4.8843	10.1108	42.4920	0.5078

To facilitate pseudo-label filtering, we introduce a classification branch as an auxiliary task that provides a proxy for assessing the reliability of regression pseudo-labels. As reported in Tables 5–7, the `regcls.-reg.` configuration achieves consistently superior performance compared with other pipelines that incorporate classification, except for on SynRS3D, where the `reg.-reg.` configuration remains competitive.

Furthermore, our experiments reveal two notable distinctions from conventional self-training frameworks designed for classification or segmentation tasks. First, both the teacher and the student must be initialized with supervision from labeled data; without such initialization, training becomes unstable and fails to converge. Second, maintaining an additional “exam” model defined as the EMA of the student yields more reliable predictions than directly relying on the teacher during inference. We denote this configuration as the Teacher–Student–Exam (TSE) pipeline, which produces to systematic improvements on ISPRS Vaihingen and GBH.

The advantages of TSE arise from two main factors. On the one hand, although the classification branch supports pseudo-label filtering, it can still interfere with the regression objective and degrade performance. On the other hand, when the teacher and student architectures differ, EMA updates do not guarantee optimal knowledge transfer. In such cases, the exam model functions as a held-out “teacher” sharing the same architecture and objective as the student. By continuously accumulating the student’s improvements through EMA, the exam model stabilizes training and maximizes the benefits of self-training during inference.

On the SynRS3D dataset, with 1% labels, the simple `reg.-reg.` pipeline already achieves competitive results. We attribute this to two factors: first, SynRS3D is a high-fidelity synthetic dataset, which facilitates pattern learning and produces reliable pseudo-labels from the teacher network. Second, the labeled split exhibits a markedly different distribution from the unlabeled, validation, and test sets. In this scenario, regression networks demonstrate stronger extrapolation capabilities than classification networks, which are less effective under distributional shifts. Notably, even though the full configuration is slightly suboptimal on SynRS3D, it still substantially outperforms the purely supervised baseline, confirming the utility of self-training in this context.

6.2. Classification

As discussed above, the classification branch underpins the pseudo-label filtering process, making its design critical to overall performance. A key consideration is how to discretize the continuous height values into classes. To this end, we compare several discretization strategies, as illustrated in Fig. 2.

From an implementation perspective, Adaptive Bins (AdaBins) defines different class boundaries for each image, which complicates cross-image comparison of class confidence and therefore undermines its suitability for pseudo-label filtering. Uniform discretization (UD) and space-increasing discretization (SID), by contrast, apply fixed binning schemes but disregard the empirical distribution of height values. When the labeled dataset is small, this often results in empty classes, increasing computational overhead without improving learning.

The results demonstrate that Hierarchical Bi-Cut (HBC) provides the most consistent performance. On both ISPRS Vaihingen and GBH, HBC achieves the lowest overall RMSEs, while also yielding balanced building RMSEs that are competitive with or superior to those obtained with UD and SID (with the only exception being a marginal drop on ISPRS Vaihingen). These findings confirm the HBC serves as a principled discretization strategy, offering both a robust class definition for pseudo-label filtering and moderate yet consistent performance gains.

6.3. Pseudo-label Filtering

Pseudo-label filtering is critical for maintaining the reliability of pseudo-labels used to train the student network. To this end, we introduce a Plackett-Luce (PL) model that explicitly aligns class probabilities with regression errors. By ranking pseudo-labels according to their predicted class confidence, the PL model enables the systematic removal of uncertain labels and thus stabilizes the learning process.

Experimental results show that incorporating the PL model consistently improves overall RMSE and class-specific RMSEs, particularly for tall land-cover categories and balanced building metrics across all datasets. These improvements demonstrate that the PL model effectively connects classification confidence with regression accuracy, especially benefiting rare or tail pixels that are otherwise susceptible to bias. Such gains enhance robustness and promote fairer performance across diverse height ranges.

However, the PL model alone is insufficient. Without ranking-based filtering, performance degrades substantially on ISPRS Vaihingen and GBH, with SynRS3D being the only exception. This suggests that while the PL model establishes a useful correlation between probabilities and errors, it can slightly impair regression performance if applied indiscriminately. Ranking-based filtering thus plays a complementary role in effectively leveraging the PL model.

Finally, because the reliability of pseudo-labels evolves during training, we employ a dynamic thresholding strategy to regulate the filtering schedule. Early in training, when the teacher lacks sufficient knowledge, only a few pseudo-labels are admitted, preventing noise from corrupting the student’s learning. As training progresses and the teacher improves, the threshold adapts to admit more pseudo-labels, thereby accelerating convergence with increasingly reliable supervision. Empirical evidence confirms the importance of this mechanism: without dynamic thresholds, ranking filtering fails entirely on ISPRS Vaihingen and GBH, highlighting its critical role in enabling pseudo-label filtering to function as intended.

7. Conclusions

In this paper, we presented TSE-Net, a self-training-based semi-supervised framework for monocular height estimation, representing the first work to address semi-supervised learning in pixel-wise regression tasks. To achieve this, we employ a multi-task regression-classification network as the teacher to facilitate pseudo-label filtering, along with a separate exam network sharing the same architecture as the student to accumulate improvements derived from student training. The teacher network incorporates a classification sub-network, with classes defined via a hierarchical bi-cut to reduce bias and enhance overall performance. Furthermore, a Plackett-Luce model aligns the pseudo-label filtering proxies, namely class probabilities, with regression errors, while a ranking-based filtering process with a dynamically evolving threshold ensures the reliability of pseudo-label selection.

As a prototypical study, our experiments demonstrate the potential of semi-supervised learning for regression tasks, achieving a performance gap reduction of up to 29.07% between models trained on 100% labeled data and only 0.1% labeled data. These results suggest that TSE-Net can be particularly beneficial for large-scale studies towards global 3D building modeling [62] where labeled data are scarce, enabling effective model training with

minimal supervision. Future work should further investigate the impact of distributional differences between labeled and unlabeled datasets on performance and explore strategies to further enhance semi-supervised regression in diverse scenarios.

References

- [1] Y. Cao, X. Huang, A deep learning method for building height estimation using high-resolution multi-view imagery over urban areas: A case study of 42 Chinese cities, *Remote Sensing of Environment* 264 (2021) 112590. [doi:10.1016/j.rse.2021.112590](https://doi.org/10.1016/j.rse.2021.112590).
- [2] Y. Cao, Q. Weng, A deep learning-based super-resolution method for building height estimation at 2.5 m spatial resolution in the Northern Hemisphere, *Remote Sensing of Environment* 310 (2024) 114241. [doi:10.1016/j.rse.2024.114241](https://doi.org/10.1016/j.rse.2024.114241).
- [3] N. Lang, W. Jetz, K. Schindler, J. D. Wegner, A high-resolution canopy height model of the Earth, *Nature Ecology & Evolution* 7 (11) (2023) 1778–1789. [doi:10.1038/s41559-023-02206-6](https://doi.org/10.1038/s41559-023-02206-6).
- [4] I. Fayad, P. Ciais, M. Schwartz, J.-P. Wigneron, N. Baghdadi, A. de Truchis, A. d'Aspremont, F. Frappart, S. Saatchi, E. Sean, A. Pellissier-Tanon, H. Bazzi, Hy-TeC: A hybrid vision transformer model for high-resolution and large-scale mapping of canopy height, *Remote Sensing of Environment* 302 (2024) 113945. [doi:10.1016/j.rse.2023.113945](https://doi.org/10.1016/j.rse.2023.113945).
- [5] H. Taubenböck, T. Esch, A. Felbier, M. Wiesner, A. Roth, S. Dech, Monitoring urbanization in mega cities from space, *Remote Sensing of Environment* 117 (2012) 162–176. [doi:10.1016/j.rse.2011.09.015](https://doi.org/10.1016/j.rse.2011.09.015).
- [6] F. Biljecki, K. A. Ohori, H. Ledoux, R. Peters, J. Stoter, Population Estimation Using a 3D City Model: A Multi-Scale Country-Wide Study in the Netherlands, *PLOS ONE* 11 (6) (2016) e0156808. [doi:10.1371/journal.pone.0156808](https://doi.org/10.1371/journal.pone.0156808).
- [7] Q. Li, S. Krapf, Y. Shi, X. X. Zhu, SolarNet: A convolutional neural network-based framework for rooftop solar potential estimation from aerial imagery, *International Journal of Applied Earth Observation and Geoinformation* 116 (2023) 103098. [doi:10.1016/j.jag.2022.103098](https://doi.org/10.1016/j.jag.2022.103098).

- [8] G. B. Bonan, Forests and Climate Change: Forcings, Feedbacks, and the Climate Benefits of Forests, *Science* 320 (5882) (2008) 1444–1449. [doi:10.1126/science.1155121](https://doi.org/10.1126/science.1155121).
- [9] G. Priestnall, J. Jaafar, A. Duncan, Extracting urban features from LiDAR digital surface models, *Computers, Environment and Urban Systems* 24 (2) (2000) 65–78. [doi:10.1016/S0198-9715\(99\)00047-2](https://doi.org/10.1016/S0198-9715(99)00047-2).
- [10] Z. Chen, H. Ledoux, S. Khademi, L. Nan, Reconstructing compact building models from point clouds using deep implicit fields, *ISPRS Journal of Photogrammetry and Remote Sensing* 194 (2022) 58–73. [doi:10.1016/j.isprsjprs.2022.09.017](https://doi.org/10.1016/j.isprsjprs.2022.09.017).
- [11] X. X. Zhu, M. Shahzad, Facade Reconstruction Using Multiview Space-borne TomoSAR Point Clouds, *IEEE Transactions on Geoscience and Remote Sensing* 52 (6) (2014) 3541–3552. [doi:10.1109/TGRS.2013.2273619](https://doi.org/10.1109/TGRS.2013.2273619).
- [12] X. X. Zhu, R. Bamler, Superresolving SAR Tomography for Multi-dimensional Imaging of Urban Areas: Compressive sensing-based TomoSAR inversion, *IEEE Signal Processing Magazine* 31 (4) (2014) 51–58. [doi:10.1109/MSP.2014.2312098](https://doi.org/10.1109/MSP.2014.2312098).
- [13] P. d’Angelo, M. Lehner, T. Krauss, D. Hoja, P. Reinartz, Towards Automated DEM Generation from High Resolution Stereo Satellite Images, in: The International Archives of the Photogrammetry, Remote Sensing and Spatial Information Sciences, International Society for Photogrammetry and Remote Sensing, Vol. XXXVII, Peking (China), 2008, pp. 1137–1342.
- [14] S. Srivastava, M. Volpi, D. Tuia, Joint height estimation and semantic labeling of monocular aerial images with CNNs, in: 2017 IEEE International Geoscience and Remote Sensing Symposium (IGARSS), 2017, pp. 5173–5176. [doi:10.1109/IGARSS.2017.8128167](https://doi.org/10.1109/IGARSS.2017.8128167).
- [15] L. Mou, X. X. Zhu, IM2HEIGHT: Height Estimation from Single Monocular Imagery via Fully Residual Convolutional-Deconvolutional Network, *arXiv:1802.10249 [cs]* (Feb. 2018). [arXiv:1802.10249](https://arxiv.org/abs/1802.10249).
- [16] P. Ghamisi, N. Yokoya, IMG2DSM: Height Simulation From Single Imagery Using Conditional Generative Adversarial Net, *IEEE Geoscience*

and Remote Sensing Letters 15 (5) (2018) 794–798. doi:10.1109/LGRS.2018.2806945.

- [17] H. A. Amirkolaei, H. Arefi, Height estimation from single aerial images using a deep convolutional encoder-decoder network, ISPRS Journal of Photogrammetry and Remote Sensing 149 (2019) 50–66. doi:10.1016/j.isprsjprs.2019.01.013.
- [18] M. Carvalho, B. Le Saux, P. Trouve-Peloux, F. Champagnat, A. Almansa, Multitask Learning of Height and Semantics From Aerial Images, IEEE Geoscience and Remote Sensing Letters 17 (8) (2020) 1391–1395. doi:10.1109/LGRS.2019.2947783.
- [19] M. Elhousni, Z. Zhang, X. Huang, Height Prediction and Refinement From Aerial Images With Semantic and Geometric Guidance, IEEE Access 9 (2021) 145638–145647. doi:10.1109/ACCESS.2021.3122894.
- [20] S. Xing, Q. Dong, Z. Hu, Gated Feature Aggregation for Height Estimation From Single Aerial Images, IEEE Geoscience and Remote Sensing Letters (2021) 1–5doi:10.1109/LGRS.2021.3090470.
- [21] X. Li, M. Wang, Y. Fang, Height Estimation From Single Aerial Images Using a Deep Ordinal Regression Network, IEEE Geoscience and Remote Sensing Letters (2020) 1–5doi:10.1109/LGRS.2020.3019252.
- [22] S. Chen, Y. Shi, Z. Xiong, X. X. Zhu, HTC-DC Net: Monocular Height Estimation From Single Remote Sensing Images, IEEE Transactions on Geoscience and Remote Sensing 61 (2023) 1–18. doi:10.1109/TGRS.2023.3321255.
- [23] Z. Xiong, W. Huang, J. Hu, X. X. Zhu, THE benchmark: Transferable representation learning for monocular height estimation, IEEE Transactions on Geoscience and Remote Sensing 61 (2023) 1–14. doi:10.1109/TGRS.2023.3311764.
- [24] Z. Xiong, F. Zhang, Y. Wang, Y. Shi, X. X. Zhu, EarthNets: Empowering artificial intelligence for Earth observation, IEEE Geoscience and Remote Sensing Magazine (2024) 2–36doi:10.1109/MGRS.2024.3466998.

- [25] Y. Ouali, C. Hudelot, M. Tami, Semi-Supervised Semantic Segmentation with Cross-Consistency Training (Jun. 2020). [arXiv:2003.09005](https://arxiv.org/abs/2003.09005), doi: [10.48550/arXiv.2003.09005](https://doi.org/10.48550/arXiv.2003.09005).
- [26] Y. Liu, Y. Tian, Y. Chen, F. Liu, V. Belagiannis, G. Carneiro, Perturbed and Strict Mean Teachers for Semi-supervised Semantic Segmentation (Mar. 2022). [arXiv:2111.12903](https://arxiv.org/abs/2111.12903), doi: [10.48550/arXiv.2111.12903](https://doi.org/10.48550/arXiv.2111.12903).
- [27] Z. Wang, Z. Zhao, X. Xing, D. Xu, X. Kong, L. Zhou, Conflict-Based Cross-View Consistency for Semi-Supervised Semantic Segmentation, in: 2023 IEEE/CVF Conference on Computer Vision and Pattern Recognition (CVPR), IEEE, Vancouver, BC, Canada, 2023, pp. 19585–19595. doi: [10.1109/CVPR52729.2023.01876](https://doi.org/10.1109/CVPR52729.2023.01876).
- [28] X. Wang, H. Bai, L. Yu, Y. Zhao, J. Xiao, Towards the Uncharted: Density-Descending Feature Perturbation for Semi-supervised Semantic Segmentation, in: 2024 IEEE/CVF Conference on Computer Vision and Pattern Recognition (CVPR), IEEE, Seattle, WA, USA, 2024, pp. 3303–3312. doi: [10.1109/CVPR52733.2024.00318](https://doi.org/10.1109/CVPR52733.2024.00318).
- [29] H. Mai, R. Sun, T. Zhang, F. Wu, RankMatch: Exploring the Better Consistency Regularization for Semi-Supervised Semantic Segmentation, in: 2024 IEEE/CVF Conference on Computer Vision and Pattern Recognition (CVPR), IEEE, Seattle, WA, USA, 2024, pp. 3391–3401. doi: [10.1109/CVPR52733.2024.00326](https://doi.org/10.1109/CVPR52733.2024.00326).
- [30] K. Sohn, D. Berthelot, N. Carlini, Z. Zhang, H. Zhang, C. A. Raffel, E. D. Cubuk, A. Kurakin, C.-L. Li, FixMatch: Simplifying Semi-Supervised Learning with Consistency and Confidence, in: Advances in Neural Information Processing Systems, Vol. 33, Curran Associates, Inc., 2020, pp. 596–608.
- [31] B. Zhang, Y. Wang, W. Hou, H. Wu, J. Wang, M. Okumura, T. Shinozaki, FlexMatch: Boosting Semi-Supervised Learning with Curriculum Pseudo Labeling (Jan. 2022). [arXiv:2110.08263](https://arxiv.org/abs/2110.08263), doi: [10.48550/arXiv.2110.08263](https://doi.org/10.48550/arXiv.2110.08263).
- [32] H. Chen, R. Tao, Y. Fan, Y. Wang, J. Wang, B. Schiele, X. Xie, B. Raj, M. Savvides, SoftMatch: Addressing the Quantity-Quality Trade-off in

Semi-supervised Learning (Mar. 2023). [arXiv:2301.10921](https://arxiv.org/abs/2301.10921), doi:10.48550/arXiv.2301.10921.

- [33] B. Sun, Y. Yang, L. Zhang, M.-M. Cheng, Q. Hou, CorrMatch: Label Propagation via Correlation Matching for Semi-Supervised Semantic Segmentation, in: 2024 IEEE/CVF Conference on Computer Vision and Pattern Recognition (CVPR), IEEE, Seattle, WA, USA, 2024, pp. 3097–3107. doi:10.1109/CVPR52733.2024.00299.
- [34] L. Yang, L. Qi, L. Feng, W. Zhang, Y. Shi, Revisiting Weak-to-Strong Consistency in Semi-Supervised Semantic Segmentation, in: 2023 IEEE/CVF Conference on Computer Vision and Pattern Recognition (CVPR), IEEE, Vancouver, BC, Canada, 2023, pp. 7236–7246. doi:10.1109/CVPR52729.2023.00699.
- [35] J. Wang, C. H. Q. Ding, S. Chen, C. He, B. Luo, Semi-Supervised Remote Sensing Image Semantic Segmentation via Consistency Regularization and Average Update of Pseudo-Label, *Remote Sensing* 12 (21) (2020) 3603. doi:10.3390/rs12213603.
- [36] B. Zhang, Y. Zhang, Y. Li, Y. Wan, H. Guo, Z. Zheng, K. Yang, Semi-supervised Deep Learning via Transformation Consistency Regularization for Remote Sensing Image Semantic Segmentation, *IEEE Journal of Selected Topics in Applied Earth Observations and Remote Sensing* 16 (2023) 5782–5796. doi:10.1109/JSTARS.2022.3203750.
- [37] Q. Li, Y. Shi, X. X. Zhu, Semi-Supervised Building Footprint Generation with Feature and Output Consistency Training, *IEEE Transactions on Geoscience and Remote Sensing* 60 (2022) 1–17. [arXiv:2205.08416](https://arxiv.org/abs/2205.08416), doi:10.1109/TGRS.2022.3174636.
- [38] X. Zhang, X. Huang, J. Li, Semisupervised Change Detection With Feature-Prediction Alignment, *IEEE Transactions on Geoscience and Remote Sensing* 61 (2023) 1–16. doi:10.1109/TGRS.2023.3247605.
- [39] W. Huang, Y. Shi, Z. Xiong, X. X. Zhu, AdaptMatch: Adaptive matching for semisupervised binary segmentation of remote sensing images, *IEEE Transactions on Geoscience and Remote Sensing* 61 (2023) 1–16.
- [40] W. Huang, Y. Shi, Z. Xiong, X. X. Zhu, Decouple and weight semi-supervised semantic segmentation of remote sensing images, *ISPRS*

Journal of Photogrammetry and Remote Sensing 212 (2024) 13–26.
doi:10.1016/j.isprsjprs.2024.04.010.

- [41] W. Huang, Z. Gu, Y. Shi, Z. Xiong, X. X. Zhu, Semi-Supervised Building Footprint Extraction Using Debiased Pseudo-Labels, *IEEE Transactions on Geoscience and Remote Sensing* 63 (2025) 1–14. doi:10.1109/TGRS.2024.3524300.
- [42] S. Chen, Y. Shi, X. X. Zhu, Long-tailed Regression with Ensembles for Monocular Height Estimation from Single Remote Sensing Images, in: 2023 Joint Urban Remote Sensing Event (JURSE), 2023, pp. 1–4. doi:10.1109/JURSE57346.2023.10144186.
- [43] R. L. Plackett, The Analysis of Permutations, *Journal of the Royal Statistical Society Series C: Applied Statistics* 24 (2) (1975) 193–202. doi:10.2307/2346567.
- [44] R. D. Luce, et al., Individual choice behavior, Vol. 4, Wiley New York, 1959.
- [45] E. Shelhamer, J. Long, T. Darrell, Fully Convolutional Networks for Semantic Segmentation, *IEEE Transactions on Pattern Analysis and Machine Intelligence* 39 (4) (2017) 640–651. doi:10.1109/TPAMI.2016.2572683.
- [46] V. Badrinarayanan, A. Kendall, R. Cipolla, SegNet: A Deep Convolutional Encoder-Decoder Architecture for Image Segmentation, *IEEE Transactions on Pattern Analysis and Machine Intelligence* 39 (12) (2017) 2481–2495. doi:10.1109/TPAMI.2016.2644615.
- [47] O. Ronneberger, P. Fischer, T. Brox, U-Net: Convolutional Networks for Biomedical Image Segmentation, *arXiv:1505.04597 [cs]* (May 2015). arXiv:1505.04597.
- [48] B. Baheti, S. Innani, S. Gajre, S. Talbar, Eff-UNet: A Novel Architecture for Semantic Segmentation in Unstructured Environment, in: 2020 IEEE/CVF Conference on Computer Vision and Pattern Recognition Workshops (CVPRW), IEEE, Seattle, WA, USA, 2020, pp. 1473–1481. doi:10.1109/CVPRW50498.2020.00187.

[49] L. Yang, B. Kang, Z. Huang, Z. Zhao, X. Xu, J. Feng, H. Zhao, Depth Anything V2 (Oct. 2024). [arXiv:2406.09414](https://arxiv.org/abs/2406.09414), doi:10.48550/arXiv.2406.09414.

[50] L. Yang, B. Kang, Z. Huang, X. Xu, J. Feng, H. Zhao, Depth Anything: Unleashing the Power of Large-Scale Unlabeled Data (Apr. 2024). [arXiv:2401.10891](https://arxiv.org/abs/2401.10891), doi:10.48550/arXiv.2401.10891.

[51] M. Oquab, T. Darcet, T. Moutakanni, H. Vo, M. Szafraniec, V. Khalidov, P. Fernandez, D. Haziza, F. Massa, A. El-Nouby, M. Assran, N. Ballas, W. Galuba, R. Howes, P.-Y. Huang, S.-W. Li, I. Misra, M. Rabbat, V. Sharma, G. Synnaeve, H. Xu, H. Jegou, J. Mairal, P. Labatut, A. Joulin, P. Bojanowski, DINOv2: Learning Robust Visual Features without Supervision (Feb. 2024). [arXiv:2304.07193](https://arxiv.org/abs/2304.07193), doi:10.48550/arXiv.2304.07193.

[52] B. Ke, K. Qu, T. Wang, N. Metzger, S. Huang, B. Li, A. Obukhov, K. Schindler, Marigold: Affordable Adaptation of Diffusion-Based Image Generators for Image Analysis (May 2025). [arXiv:2505.09358](https://arxiv.org/abs/2505.09358), doi:10.48550/arXiv.2505.09358.

[53] H. Fu, M. Gong, C. Wang, K. Batmanghelich, D. Tao, Deep Ordinal Regression Network for Monocular Depth Estimation, in: 2018 IEEE/CVF Conference on Computer Vision and Pattern Recognition, IEEE, Salt Lake City, UT, 2018, pp. 2002–2011. doi:10.1109/CVPR.2018.00214.

[54] S. F. Bhat, I. Alhashim, P. Wonka, AdaBins: Depth Estimation using Adaptive Bins, in: 2021 IEEE/CVF Conference on Computer Vision and Pattern Recognition (CVPR), 2021, pp. 4008–4017. [arXiv:2011.14141](https://arxiv.org/abs/2011.14141), doi:10.1109/CVPR46437.2021.00400.

[55] S. F. Bhat, I. Alhashim, P. Wonka, LocalBins: Improving Depth Estimation by Learning Local Distributions (Mar. 2022). [arXiv:2203.15132](https://arxiv.org/abs/2203.15132), doi:10.48550/arXiv.2203.15132.

[56] Z. Li, X. Wang, X. Liu, J. Jiang, BinsFormer: Revisiting Adaptive Bins for Monocular Depth Estimation, IEEE Transactions on Image Processing 33 (2024) 3964–3976. doi:10.1109/TIP.2024.3416065.

[57] R. Herbrich, T. Graepel, K. Obermayer, Support vector learning for ordinal regression, in: 1999 Ninth International Conference on Artificial

Neural Networks ICANN 99. (Conf. Publ. No. 470), Vol. 1, 1999, pp. 97–102 vol.1. doi:10.1049/cp:19991091.

[58] F. E. Harrell, Regression Models for Continuous Y and Case Study in Ordinal Regression, in: Jr. Harrell, Frank E. (Ed.), Regression Modeling Strategies: With Applications to Linear Models, Logistic and Ordinal Regression, and Survival Analysis, Springer International Publishing, Cham, 2015, pp. 359–387. doi:10.1007/978-3-319-19425-7_15.

[59] 2D Semantic Label. - Vaihingen.

[60] B. Le Saux, N. Yokoya, R. Haensch, M. Brown, 2019 IEEE GRSS Data Fusion Contest: Large-Scale Semantic 3D Reconstruction [Technical Committees], IEEE Geoscience and Remote Sensing Magazine 7 (4) (2019) 33–36. doi:10.1109/MGRS.2019.2949679.

[61] J. Song, H. Chen, W. Xuan, J. Xia, N. Yokoya, SynRS3D: A Synthetic Dataset for Global 3D Semantic Understanding from Monocular Remote Sensing Imagery (Jun. 2024). arXiv:2406.18151.

[62] X. X. Zhu, S. Chen, F. Zhang, Y. Shi, Y. Wang, Globalbuildingatlas: An open global and complete dataset of building polygons, heights and lod1 3d models, Earth System Science Data Discussions 2025 (2025) 1–31. doi:10.5194/essd-2025-327.
URL <https://essd.copernicus.org/preprints/essd-2025-327/>